

Cite this: *J. Mater. Chem. A*, 2020, **8**, 3499

Nickel nanograins anchored on a carbon framework for an efficient hydrogen evolution electrocatalyst and a flexible electrode†

Zhiwei Zhang,^a Linjie Deng,^b Zhe Zhao,^a Yuting Zhao,^a Jingyu Yang,^a Jun Jiang,^a ^{*b} Gaoshan Huang ^{*a} and Yongfeng Mei ^a

The atomic layer deposition (ALD) technique has been widely employed in the development of efficient electrochemical hydrogen evolution reaction (HER) catalysts. Nevertheless, most of the studies through this methodology are confined to the use of precious metals or non-precious materials with poor performance, especially in alkaline electrolytes. Herein, we report a novel strategy of fabricating nickel nanograins coated onto a Co, N-doped carbon framework (Co-NCF@Ni) based on the manipulation of ALD and *in situ* transformation of a cobalt zeolitic imidazolate framework for efficient hydrogen evolution in alkaline media. The catalytic performance of the Co-NCF@Ni with different Ni contents is specifically studied. On the basis of this composite, a flexible high-performance H₂ production device, distinguished from the conventional powdery pattern, is realized, and stable performance under a repeated rolling process is demonstrated. In order to disclose the mechanism of the remarkable HER performance, density functional theory calculations are carried out and the results indicate that the electron structures of inner Co atoms, external Ni atoms, and the N-doped carbon layer can be tuned due to the introduction of Ni nanoparticles. The research presented here may have great potential in developing both high efficiency transition-metal based electrocatalysts and flexible H₂-production devices for use under extreme conditions.

Received 12th December 2019
Accepted 16th January 2020

DOI: 10.1039/c9ta13632k

rsc.li/materials-a

1 Introduction

Hydrogen has been considered a sustainable clean energy to replace fossil fuels because of its high efficiency and pollution-free production.^{1–4} At present, hydrogen generation *via* electrochemical water splitting has become an intriguing and productive approach, in which an efficient catalyst for the hydrogen evolution reaction (HER) is crucial for its indispensable capability of actuating the multi-step reaction.⁵ So far, catalysts based on precious metals such as Pt and Ir which exhibit excellent performance have been used.^{6,7} Unfortunately, the large utilization of these noble-metal based catalysts has been severely hindered due to their scarce earth abundance and high cost. Therefore, a wide spectrum of compounds based on transition metals (TMs) (*e.g.*, alloys, dichalcogenides, phosphides, carbides, and nitrides) have been investigated for the possibility of using them as alternatives to precious-metal-

based catalysts over the past decade.^{8–11} However, most of the TM-based catalysts are readily corroded in acidic environments which comparatively narrows the application of these materials in both the HER and proton exchange membrane fuel cells.¹² Consequently, numerous efforts are devoted to developing efficient and stable electrocatalysts in alkaline electrolytes in order to promote the commercialization of hydrogen production.¹³

On the other hand, metal-organic frameworks (MOFs), which are constructed from certain metal ions and organic ligands, are emerging as promising precursors to prepare TM-based electrochemical HER catalysts in different electrolytes because of the N-doping and the introduction of various metal ions.^{14–18} Nevertheless, most MOF-derived electrocatalysts improve the catalytic performance monotonically due to the introduction of multiple metal ions into the inner hollow structure, which cannot get rid of the carbon shell trap, leading to the coverage of numerous metal surface active sites.¹⁹ In addition, only a few reaction mechanisms providing deep insight into MOF-derived electrocatalysts have been studied because of the complexity of metal doping inside the carbon framework.²⁰

To tackle the challenge associated with MOF-derived catalysts for the HER, we found that the utilization of atomic layer deposition (ALD) to deposit active materials with precisely

^aDepartment of Materials Science, Fudan University, Shanghai 200433, China. E-mail: gshuang@fudan.edu.cn

^bHefei National Laboratory for Physical Sciences at the Microscale, School of Chemistry and Materials Science, University of Science and Technology of China, Hefei 230026, China. E-mail: jiangj1@ustc.edu.cn

† Electronic supplementary information (ESI) available. See DOI: 10.1039/c9ta13632k

controlled size on the surface is beneficial for simplifying the preparation.^{21–23} Some progress has been achieved *via* this approach. For instance, Lei *et al.*²⁴ have synthesized carbon nanofibers with Pt particles deposited by ALD which could reach an overpotential of 55 mV at 10 mA cm⁻² in 0.5 M H₂SO₄. Cheng and co-workers demonstrated that single Pt atoms and clusters synthesized by ALD supported on N-doped graphene nanosheets could deliver 10 mA cm⁻² at an overpotential of ~38 mV in acidic media.²⁵ Nayak *et al.*²⁶ reported that laser scribed graphene with atomic layer deposited Pt could achieve an overpotential of 131 mV at 10 mA cm⁻² in acidic electrolytes. Kim *et al.*²⁷ modified the surface of MoS₂ with TiO₂ by utilizing the ALD technique and developed a self-supporting electrode for the HER. Kim and co-workers prepared cobalt sulfide by low-temperature ALD which showed a low Tafel slope of 41 mV dec⁻¹ and high exchange current density.²⁸ Moreover, previous studies in the literature have proved that incorporated transition metals can tune the surface electronic structure and change the adsorption energies toward optimal electrocatalytic activity.^{29,30} The advantage of the ALD method can also help us to construct efficient electrocatalysts with controllable structures and analyze the local charge change of the active sites and its natural influence on the catalytic performance, which may provide a great chance to alter the catalytic activity.³¹ However, although continuous progress has been achieved in this field, most electrocatalysts fabricated by this approach still suffer from some major drawbacks including the extensive use of precious metals, the low catalytic performance especially in alkaline electrolytes, and the low mass loading due to the powdery pattern of the catalyst. These drawbacks could seriously hinder the practical application and commercialization of the catalysts.

To address the aforementioned challenges and chances, herein, we prepared a novel hybrid nanostructure composed of a Co, N-doped carbon framework (Co-NCF) coated with nickel nanograins through a facile pyrolysis–ALD strategy. The introduction of Ni nanograins was proved to efficiently enhance the HER performance of the matrix. While some previous literature studies reported that the doping of specific transition metals like Co/Ni,³² Fe/Co,³³ Zn/Ni,³⁴ and even on a carbon substrate (Ni–C)³⁵ could positively influence the catalytic results, we here would like to exhibit a new route for the external anchoring of elemental nickel nanograins by utilizing ALD. In this pyrolysis–ALD approach, a Co-NCF derived from a cobalt zeolitic imidazolate framework (ZIF-67) was used as a matrix for the ALD of Ni nanoparticles. Different ALD cycles (*e.g.*, 100, 400, and 600 cycles) were engaged to produce a Ni coated Co-NCF (Co-NCF@Ni) with controllable size and distribution of Ni nanograins. The Co-NCF@Ni composite with 600 ALD cycles (Co-NCF@600-Ni) exhibits a superior electrochemical performance with a low overpotential of 157 mV at 10 mA cm⁻² and 20 h long-term durability. Moreover, inspired by the superior properties such as large surface area, high portability, and great versatility of flexible devices in electronics and energy conversion applications,^{36–39} we designed a flexible HER electrode which is constructed by painting Co-NCF@600-Ni slurry onto soft carbon fiber paper (CFP). The electrochemical performance of the

flexible devices was studied under different curvatures and various rolling times. The device demonstrated an overpotential of 160 mV (10 mA cm⁻²) under a strain of ~0.0066 and a slight performance attenuation even after 50 times repeated rolling. This work provides a tactic for producing highly efficient HER catalysts based on ALD, which can be assembled as deformable electrodes with high performance and may have great potential in fabricating numerous flexible devices for future energy conversion systems under complex circumstances.

2 Experimental

2.1 Synthesis of ZIF-67 and the Co-NCF

All the chemicals were of analytical grade and used without further purification. In a typical procedure of synthesis of ZIF-67, 1.642 g 2-methylimidazole (2-MeIm) and 1.455 g Co(NO₃)₂·6H₂O were dissolved in a mixed solution of 40 mL methanol and 40 mL ethanol. Then the solution of 2-MeIm was subsequently poured into the solution of Co(NO₃)₂·6H₂O. Following that, the mixed solution was vigorously stirred for at least 5 min and was subsequently left to stand still for 24 h at room temperature. After that, the purple precipitate was centrifuged and washed with methanol three times and dried at 60 °C in air for 24 h. The prepared ZIF-67 was then placed in a tube furnace, heated to 700 °C (1 °C min⁻¹), and kept for 1 h in a N₂ atmosphere. Finally, the ZIF derived Co-NCF was obtained.

2.2 ALD synthesis of Co-NCF@Ni

Ni was deposited on the Co-NCF by ALD (MNT f-150-212, MNT Micro and Nanotech Co., LTD, China) with Ni(acac)₂(tmeda) and anhydrous hydrazine (N₂H₄) as precursors. High purity N₂ (99.999%) was utilized as both the carrier gas and the purging gas. The black Co-NCF powder was placed in an open container inside the ALD chamber. Ni(acac)₂(tmeda) and N₂H₄ were, respectively, kept at 100 and 50 °C to provide steady fluxes of precursor gases. The deposition temperature was 200 °C and the working pressure was kept at 50–60 Pa. For each ALD cycle, a Ni(acac)₂(tmeda) pulse for 1 s and an N₂H₄ pulse for 0.2 s were separated by a 20 s N₂ pulse. Different numbers of ALD cycles were performed to investigate the influence on the structure of the Ni nanograins.

2.3 Fabrication of the Co-NCF@600-Ni/CFP flexible electrode

A CFP belt (1 cm × 25 cm × 0.03 cm) was first washed with ethanol and deionized water to remove the impurity on the surface and then dried at 60 °C in a vacuum for 1 h. Next, a PET belt (0.9 cm × 25 cm × 0.01 cm) was adhered onto the backside of the CFP with polyimide glue to support the thin CFP. Then, 1.6 mg Co-NCF@600-Ni powder, 0.2 mg graphite, and 4 mg polyvinylidene fluoride (5 wt%) were mixed together in a weight ratio of 8 : 1 : 1 to form a uniform colloid-like mixture with the addition of a moderate amount of *N*-methyl-2-pyrrolidone. The obtained black slurry was subsequently cast on the blank side of the pretreated CFP belt in an area of 10 mm × 20 mm with a mass loading of ~0.8 mg cm⁻². After that, Co-NCF@600-Ni/

CFP was obtained after the belt was dried at 60 °C in a vacuum for 24 h. The fabricated catalyst belt was rolled onto Teflon rods with different diameters for the HER test. Notably, the same Co-NCF@600-Ni/CFP belt should be tested to exclude other interferences except the change of curvature.

2.4 Characterization

The morphologies and structures were characterized by field-emission SEM (Nova NanoSem 450) and HRTEM (Tecnai G2 F20 S-Twin). XRD was carried out with a D8 ADVANCE X-ray diffractometer with Cu K α radiation ($\lambda = 1.5406 \text{ \AA}$) to study the crystallographic structure. XPS was carried out on an Axis Ultra DLD spectrometer with a Mg K α radiation source. Raman spectra were recorded using a Horiba LabRAM Jobin Yvon HR-Evolution 2 apparatus.

2.5 Electrochemical measurements

All the electrochemical measurements were conducted on a CHI660E electrochemical workstation (Chenhua Instrument, Shanghai, China) by using a conventional three-electrode cell in a N₂-saturated 1 M KOH electrolyte at ~20 °C. Carbon rod and Ag/AgCl (3 M KCl) electrodes served as the counter electrode and reference electrode, respectively. To test the performance of the catalyst in powder form, in a typical process, 4 mg catalyst was dispersed in a mixture of 970 μL ethanol and 30 μL Nafion (5 wt%, Sigma-Aldrich) under ultrasonication for 40 min. Then, 5 μL of the dispersion ink was dropped onto a GCE with a diameter of 3 mm, serving as the working electrode with a mass loading of ~0.28 mg cm⁻². For the flexible Co-NCF@Ni/CFP, the prepared catalyst belt was rolled onto Teflon rods with different diameters (10 mm, 20 mm, and 30 mm) but the same length of 50 mm and then used as the working electrode. LSV was carried out at a scan rate of 5 mV s⁻¹ in the range of -0.8 to -1.6 V. CV measurements were performed at a non-faradaic region to estimate the electrochemical double layer capacitance (C_{dl}). EIS measurement was carried out in the frequency range of 10⁻² to 10⁶ Hz with an amplitude of 5 mV. All potentials were calibrated to the reversible hydrogen electrode (RHE) via the Nernst equation as follows: $E_{\text{RHE}} = E_{\text{Ag/AgCl}} + 0.0592\text{pH} + E_{\text{Ag/AgCl}}^{\ominus}$. The catalytic stability was evaluated by using both the chronoamperometric response and potential cycles in 1 M KOH N₂-saturated solution. All the collected data were corrected for *iR*-compensation.

2.6 DFT calculations

Periodic density functional theory (DFT) calculations were carried out by using the Perdew–Burke–Ernzerhof (PBE)^{40,41} functional and the plane-wave projected augmented wave (PAW)⁴² method as implemented in the Vienna *Ab initio* Simulation Package (VASP).^{43–46} An energy cutoff of 400 eV was used for the plane-wave expansion of the electronic wave function. We adopted a 4 × 4 × 1 supercell model of graphene with the lattice constants of $a = b = 9.8318 \text{ \AA}$ and $c = 20 \text{ \AA}$. Four different models of the support were considered, including pure graphene (C), Co particles encapsulated in nitrogen doped graphene (Co@NC), Co particles encapsulated in nitrogen doped

graphene with half number of Ni atoms anchored (Co@NC@Ni (2 : 1)), and similar structures with equal number of Ni atoms (Co@NC@Ni (1 : 1)). The Monkhorst–Pack⁴⁷ sampling scheme of the Brillouin zone was adopted to generate 3 × 3 × 1 *k*-point grids. The whole system was fully optimized with convergence criteria of 1 × 10⁻⁴ eV for total energy and 0.02 eV \AA^{-1} for the maximum force on each atom.

3 Results and discussion

The schematic of the synthetic process of Co-NCF@Ni is depicted in Fig. 1a. First, dodecahedral ZIF-67 (see also Fig. 1b) was synthesized by a common solvothermal reaction using Co(NO₃)₂·6H₂O as a Co ion source and 2-MeIm as an organic ligand at room temperature.⁴⁸ Then, the Co-NCF was prepared by direct pyrolysis of the ZIF-67 under a N₂ flow at 700 °C for 1 h. During the thermal treatment process, the Co ions were reduced to metallic Co nanoparticles while the coordinated organic framework was converted to a N-doped carbon framework and the dodecahedron geometry was largely maintained (Fig. 1c). The *in situ* formation of the N-doped carbon framework (NCF) could significantly restrict the aggregation of the inner Co nanoparticles which could expose more active sites for the HER. Following that, Ni nanograins were deposited onto the Co-NCF by the ALD process using Ni(acac)₂(tmeda) and N₂H₄ as the Ni source and reduction gas, respectively, at a low chamber temperature of 200 °C.⁴⁹ Benefiting from the low deposition temperature of ALD, the eventually obtained Co-NCF@Ni retained the dodecahedron shape which can provide a stable host matrix for both inner Co nanoparticles and external Ni nanograins (Fig. 1d). Moreover, Ni was deposited with various ALD cycles of 100, 400, and 600 to tune the size and distribution of the Ni nanograins. As presented in Fig. 1d and S1,[†] the scanning electron microscopy (SEM) images of Co-NCF@100-Ni, Co-NCF@400-Ni, and Co-NCF@600-Ni not only reveal that the catalysts retain the homogeneous morphology but also that small Ni nanograins anchor on the surface of the Co-NCF, leading to a rougher surface compared with the bare Co-NCF. In order to further investigate the morphology and diversity of Ni nanoparticles produced by ALD, a Si substrate was used as the reference. Morphological characterization demonstrates that the deposition of Ni on the Si substrate (Fig. S2[†]) also gives it the characteristic granular appearance. The size distribution analyses (inset of Fig. S2[†]) reveal that the average sizes of the nanoparticles deposited with 100, 400, and 600 ALD cycles are approximately 6, 21, and 29 nm, respectively. Fig. 1e summarizes the ALD procedure and the particle size as a function of the number of ALD cycles, demonstrating a good capability of the current approach to tune the particle size.

In order to determine the phase of the conversion, powder X-ray diffraction (XRD) patterns were studied. The patterns of violet ZIF-67 powder and black Co-NCF powder (Fig. S3[†]) indicate the complete conversion from ZIF-67 to the carbon framework and the formation of elemental Co particles. The Raman spectra of the Co-NCF and Co-NCF@Ni (Fig. S4[†]) provide evidence that the organic framework is radically carbonized after the pyrolysis, as D and G bands were noticed at

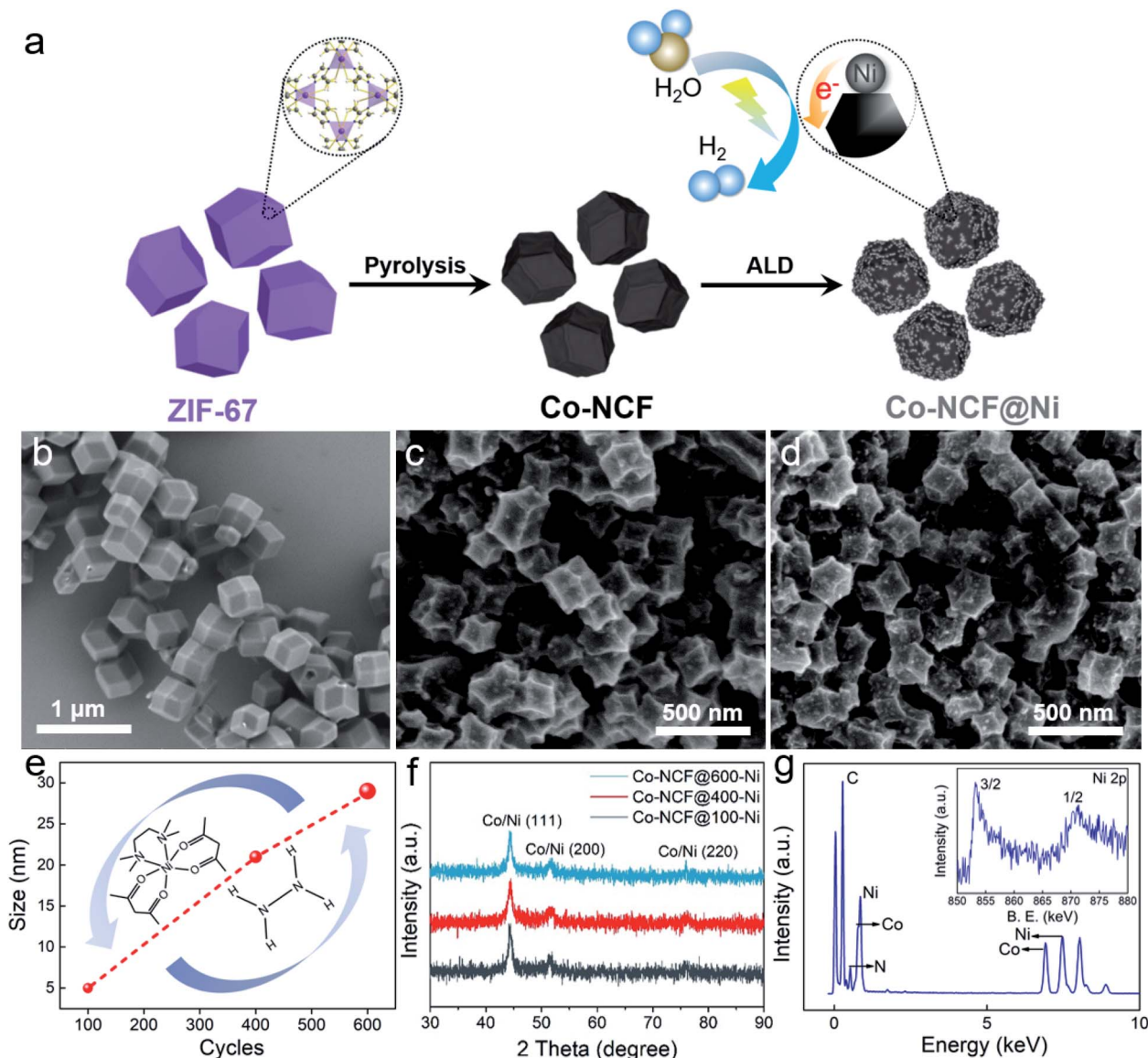


Fig. 1 (a) Schematic illustration of the synthesis process of the Co-NCF@Ni composite. SEM images of (b) ZIF-67, (c) Co-NCF, and (d) Co-NCF@600-Ni. (e) Ni particle size controllability as a function of the number of ALD cycles (the inset demonstrates the chemical formula of the two precursors for the ALD process: Ni(acac)₂(tmeda) and N₂H₄). (f) XRD patterns and (g) EDX spectrum of Co-NCF@600-Ni. Inset: Ni 2p XPS spectrum of Co-NCF@600-Ni.

1351 and 1592 cm⁻¹, respectively. Additionally, Fig. 1f shows the XRD patterns of three Co-NCF@Ni samples. It can be noted that only the metallic fcc Co and Ni can be observed without other phases.^{49,50} X-ray photoelectron spectroscopy (XPS) was utilized to further examine the composition of the catalysts. The spectra of the Co-NCF (Fig. S5†) suggest the full reduction of Co ions after the pyrolysis and the formation of electrochemically active Co-N bonds.⁵¹ However, for Co-NCF@Ni, the similar C 1s, N 1s, and Co 2p spectra (Fig. S6†) demonstrate that the ingredients of the Co-NCF are immune to the process of ALD because of the low reaction temperature and the self-limited growth process. Fig. 1g shows the EDX spectrum of Co-NCF@600-Ni which indicates a relatively high nickel content, with the detailed atomic percentages of the elements shown in

Table S1.† The existence of Ni in the Co-NCF@Ni composites is proved by the Ni 2p spectra presented in the inset of Fig. 1g and S7.† Ni 2p_{3/2} peaks at ca. 853.1 eV and Ni 2p_{1/2} peaks at ca. 870.2 eV can be clearly observed in all three spectra, indicating the metallic status of Ni, which is consistent with the XRD results.

High-resolution transmission electron microscopy (HRTEM) and energy dispersive X-ray (EDX) elemental mapping were carried out to further determine the microstructural properties of the composite. As shown in Fig. 2a and b, the TEM images of Co-NCF@600-Ni indicate that almost all catalytic units maintain an intact dodecahedron framework whose porous structure could be beneficial to the HER process,⁵² and the Ni nanograins anchored on the NCF are obvious. The EDX mapping (Fig. 2c-f)

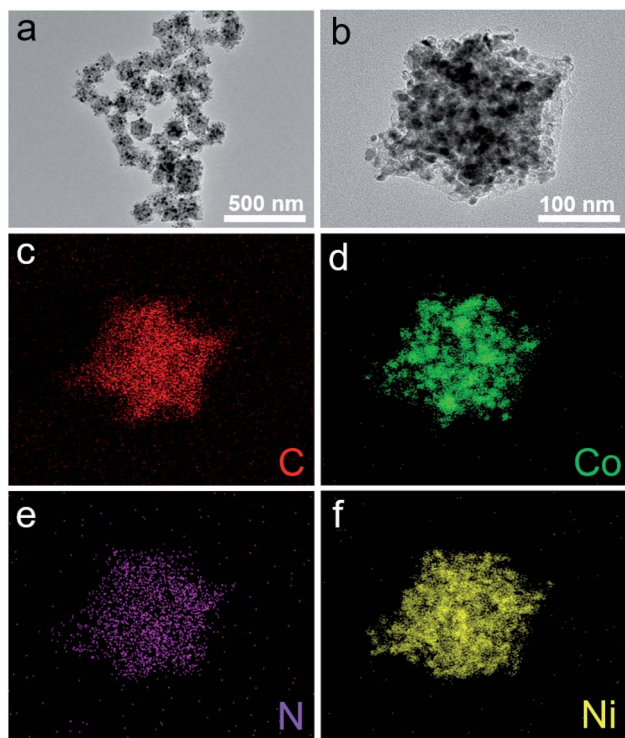


Fig. 2 (a and b) TEM images of the Co-NCF@600-Ni composite. (c–f) Corresponding EDX mapping images of the composite in (b), showing the presence of (c) C, (d) Co, (e) N, and (f) Ni.

images corresponding to Fig. 2b clearly demonstrate that C, N, Co, and Ni are evenly distributed over the entire Co-NCF@600-Ni composite structure, suggesting a homogeneous integration

of Ni. The TEM images and corresponding EDX mapping of the Co-NCF, Co-NCF@100-Ni, and Co-NCF@400-Ni, with elemental constituent contents, are clearly shown in Fig. S9, S10, and S11,[†] respectively. It can be noted that the Ni content increases as the number of ALD cycles increases because more Ni is deposited on the framework during the ALD process.

The electrocatalytic performance of the as-prepared Co-NCF and Co-NCF@Ni with different ALD cycles was examined for the HER by using a three-electrode system in N₂-saturated 1 M KOH, and a mass loading of 0.28 mg cm⁻² was adopted for all the samples. Linear sweep voltammetry (LSV) was first performed at a scan rate of 5 mV s⁻¹. As illustrated in Fig. 3a, a bare glassy carbon electrode (GCE) and a commercial Pt/C electrode (5%, Sigma-Aldrich) were also measured as references. In order to achieve a current density of 10 mA cm⁻², the Co-NCF@600-Ni shows a lower overpotential (157 mV) than Co-NCF@400-Ni (168 mV), Co-NCF@100-Ni (243 mV), and Co-NCF (286 mV), while the GCE shows far more than 500 mV and the Pt/C electrode shows 57 mV. The results reveal that the deposition of Ni particles on the Co-NCF by ALD could effectively enhance the electrocatalytic activity. In addition, it is worth noting that the performance of Co-NCF@Ni is better than that of the Ni-C composite reported in the literature.³⁵ The reason is considered to be the active sites provided by the interfaces between the coated Ni and the Co-NCF. And Co-NCF@600-Ni with more Ni nanograins consequently demonstrates the highest HER catalytic performance in alkaline electrolytes. Notably, as exhibited in Table 1, when compared with most of the reported non-precious catalysts based on vapor reactions such as ALD or chemical vapor deposition (CVD), our Co-NCF@600-Ni shows a remarkably enhanced catalytic performance in alkaline solution.

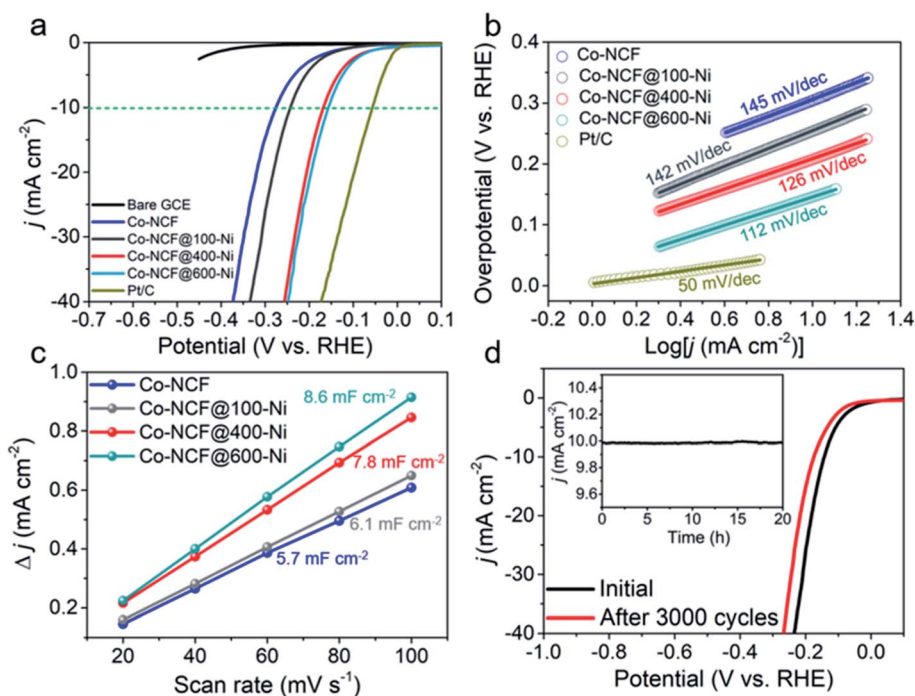


Fig. 3 (a) LSV curves and (b) Tafel curves of the Co-NCF, Co-NCF@100-Ni, Co-NCF@400-Ni, Co-NCF@600-Ni, and commercial Pt/C. (c) C_{dl} values of the Co-NCF, Co-NCF@100-Ni, Co-NCF@400-Ni, and Co-NCF@600-Ni electrodes. (d) HER stability tests of the Co-NCF@600-Ni.

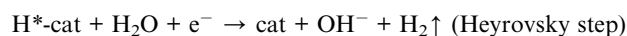
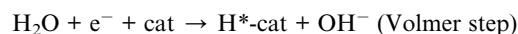
Table 1 Comparison of the electrolytic HER performance of Co-NCF@600-Ni with that of other non-precious metal electrocatalysts based on ALD or CVD

Catalyst	Methods	Electrolyte	Overpotential at 10 mA cm ⁻²	Reference
ALD (TiO ₂)-MoS ₂	ALD	0.5 M H ₂ SO ₄	Over 300 mV	53
Ni ₃ S ₂ /Au; Ni ₃ S ₂ /SiO ₂	ALD	1.0 M KOH	~300 mV	54
MoS ₂ /Au foil	CVD	0.5 M H ₂ SO ₄	~200 mV	55
MoSe ₂ /CC	CVD	0.5 M H ₂ SO ₄	Over 200 mV	56
TiS ₂ QDs	ALD	0.5 M H ₂ SO ₄	245 mV	57
Mo-thiolate	ALD	0.5 M H ₂ SO ₄	294 mV	58
MoS ₂	ALD	0.5 M H ₂ SO ₄	Over 250 mV	59
MoS ₂ /MoSe ₂	CVD	0.5 M H ₂ SO ₄	Over 300 mV	60
CoS _x /GF, CoS _x /CT	ALD	NA	295 mV, 265 mV	61
Co-NCF@600-Ni	ALD	1.0 M KOH	157 mV	This work

Here, Tafel slopes were calculated by linearly fitting the polarization curves to evaluate the HER kinetics of the catalysts. As presented in Fig. 3b, the Tafel slope of Co-NCF@600-Ni is 112 mV dec⁻¹, which is less than the 126 mV dec⁻¹ for Co-NCF@400-Ni, 142 mV dec⁻¹ for Co-NCF@100-Ni, and 145 mV dec⁻¹ for Co-NCF, indicating an enhancement of HER kinetics by the ALD-Ni coating. Such a Tafel slope of Co-NCF@600-Ni suggests that a combined Volmer-Heyrovsky reaction mechanism dominates the HER process, and the electrochemical desorption is the rate-determining step, based on the classical three principal steps (Volmer, Heyrovsky, and Tafel steps) for the HER in alkaline electrolytes.⁶²⁻⁶⁴ Electrochemical impedance spectroscopy (EIS) was used to further investigate the catalytic kinetics. As illustrated in Fig. S12,† the Nyquist plots and the fitting results of the Co-NCF electrode and Co-NCF@Ni electrodes show linear traits in low-frequency regions and no obvious semicircles are observed in their high-frequency regions, suggesting their strong electron-transfer ability.⁶⁵⁻⁶⁷ In order to examine the electrochemically active surface area, for which a higher value usually means more potential active sites for catalysis, the capacitance of the double layer (C_{dl}) at the electrode-electrolyte interface was tested by cyclic voltammetry (CV) in the range of 20–100 mV (Fig. S13†). Fig. 3c shows that the C_{dl} of the Co-NCF@600-Ni electrode is 8.6 mF cm⁻² which is derived from the CV measurements (Fig. S13†). Additionally, the C_{dl} values of Co-NCF@400-Ni (7.8 mF cm⁻²), Co-NCF@100-Ni (6.1 mF cm⁻²) and Co-NCF (5.7 mF cm⁻²) were also calculated from the CV test (Fig. S13†). It is apparent that the Co-NCF@600-Ni possesses the highest C_{dl} value, implying the most number of active sites, which is in accordance with the analysis of the LSV curves. Stability is also a critically important property of electrocatalysts. The stability of Co-NCF@600-Ni was measured by running long-term CV cycles at a scan rate of 100 mV s⁻¹ and potential-constant electrolysis. As presented in Fig. 3d, the polarization curve of the Co-NCF@600-Ni recorded after 3000 cycles shows a small increase of overpotential (~30 mV) at 10 mA cm⁻², indicating good durability of the catalyst. Moreover, a chronoamperometry test (inset of Fig. 3d) also indicated excellent stability of the composite with only a slight deactivation after a continuous 20 h test. The morphology (Fig. S14†) and the XRD pattern (Fig. S15†) of the sample after the 20 h chronoamperometry test almost

retain the original dodecahedron structure and the crystal structure, respectively, further suggesting the superior stability of Co-NCF@600-Ni.

In order to gain atomic-scale understanding of the catalytic nature of the Co-NCF@Ni, we carried out density functional theory (DFT) calculations which provided a fundamental understanding of the enhanced HER activity of Co-NCF@600-Ni on the atomic scale. Several theoretical models including graphene (C), Co particles encapsulated in nitrogen doped graphene (Co@NC), Co particles encapsulated in nitrogen doped graphene (NC) with half number of Ni atoms anchored (Co@NC@Ni (2 : 1)), and similar structures with equal number of Ni atoms (Co@NC@Ni (1 : 1)) were employed here. Particularly, the model was constructed with an identical number of Co and Ni atoms so that the system could match the elemental distribution results of EDX mapping of the Co-NCF@600-Ni sample, which is presented in Fig. 2c–f and Table S1,† while the model of Co@NC@Ni (2 : 1) represents the Co-NCF@400-Ni sample. In alkaline solution, the H₂O dissociation-adsorption should be considered in the HER.⁶⁸ The reaction mechanism of an alkaline HER follows three key steps:



The free energy for the first step and third step is supposed to be the same at the equilibrium potential of the HER. Under this assumption, one can avoid computation of the exact free energy of OH⁻ in solution by using a computational hydrogen electrode.⁶⁹ In this way, four stages should be considered in an alkaline HER: the initial stage, activated H₂O adsorption, H* intermediate formation, and H₂ formation.⁷⁰ The $\Delta G_{\text{H}_2\text{O}}$ and ΔG_{H^*} are widely applied as activity descriptors for understanding HER catalytic activity. The $\Delta G_{\text{H}_2\text{O}}$ value is utilized for the free energy difference between the first and second stage. The ΔG_{H^*} value is applied as the free energy difference between the third and fourth stage.^{70,71} And the species H-OH is a ground state of activated water adsorption. It should be noted that free energies close to zero indicate that the transition

processes can take place easily.^{72–74} As shown in Fig. 4a, with regard to the energy barrier of H₂O dissociation $\Delta G(\text{H}_2\text{O})$, the bare pristine graphene showed an extremely high value of 4.26 eV, which mainly prevents the dissociation of H₂O to H* and induces lower HER kinetics. With one single metal or double transition metals doped into the catalysts, $\Delta G(\text{H}_2\text{O})$ was reduced to 2.48 eV for Co@NC, 2.78 eV for Co@NC@Ni (2 : 1) and 2.20 eV for Co@NC@Ni (1 : 1). On the other hand, we note that the $\Delta G(\text{H}^*)$ of Co@NC (0.640 eV) is much higher than that for the Co@NC@Ni (2 : 1) (0.255 eV). Previous literature studies have concluded that the kinetics of the HER in alkaline solution depend on both the Volmer step and Heyrovsky step, and both the water dissociation barrier energy and the hydrogen adsorption energy collectively influence the HER performance.^{75,76} Therefore, taking $\Delta G(\text{H}_2\text{O})$ and $\Delta G(\text{H}^*)$ into account, Co@NC@Ni (1 : 1) holds a lower systematic energy barrier than Co@NC and Co@NC@Ni (2 : 1). This is in accordance with the experimental results shown in Fig. 3. Here, the schematic representation of the four-stage reaction of Co@NCF@Ni (1 : 1), which is the best electrocatalyst, is shown in Fig. 4b.

To further clarify the electron transfer process, we also calculated the charge transfer of C–H, Co@NC–H, Co@NC@Ni (2 : 1)–H, and Co@NC@Ni (1 : 1)–H systems (Fig. 4c and S16†). When Co atoms are introduced, some negative charges transfer from Co to C. Once Ni nanograins are loaded onto the system, the weak charge transfer between Co and C atoms is slightly enhanced. In conclusion, the binding strength between graphene and H can be enhanced by different means, including the encapsulation of Co clusters, and the loading of Ni nanograins on graphene. Further, the HER activity is promoted as well.⁷⁷ In short, DFT results indicate that various chemical modifications at the interfaces (*i.e.*, Co/NCF/Ni interfaces) are an effective means to generate new active sites and reduce the overpotential of the HER, which demonstrates the high catalytic performance of current composites.

In addition, encouraged by the unique structure of the Co-NCF@600-Ni composite and its excellent HER performance in powder form, we proposed to build a flexible device aiming to

enhance the mass loading and realize the functionality of the catalysts in complex and extreme environments *e.g.*, buckling and bending geometries. As shown in Fig. S17,† we designed a flexible device which is constructed using a Teflon rod and a piece of carbon fiber paper (CFP) painted with the Co-NCF@600-Ni composite (see the Experimental section). Three Teflon rods (diameters: 10 mm, 20 mm, and 30 mm) were adopted as moulds to investigate the HER performance of the Co-NCF@600-Ni/CFP under different rolling strains. The radian angle value θ of each device was first calculated using the circle equation:

$$\theta = L/R, \quad (1)$$

where L is the belt length which here is a constant of 20 mm because of the catalyst area covering a region of 10 mm × 20 mm and R is the radius (here 5.2 mm, 10.2 mm and 15.2 mm, respectively, taking the thickness of polyethylene terephthalate (PET) and the CFP substrate into consideration). Then, the strains of Co-NCF@600-Ni/CFP rolling onto the rods were calculated approximately based on the bending strain equation:⁷⁸

$$\varepsilon = \frac{(\rho + y)d\theta - \rho d\theta}{\rho d\theta}, \quad (2)$$

where ρ is the radius of curvature of the neutral layer and y is the neutral layer to boundary distance (Fig. S18†). The obtained strains were about 0.0192, 0.0098, and 0.0066, respectively, corresponding to rods with diameters of 10, 20, and 30 mm (Table S2†).

The electrocatalytic performances of the flexible Co-NCF@600-Ni/CFP electrode with different statuses were studied by the HER test in N₂-saturated 1 M KOH aqueous electrolyte, and the rolled belts on Teflon rods were directly used as working electrodes. A pristine CFP belt and a catalyst belt in the flat state before rolling were measured for comparison. During the electrolysis, a large number of H₂ bubbles were produced from the Co-NCF@600-Ni catalyst area on the belt

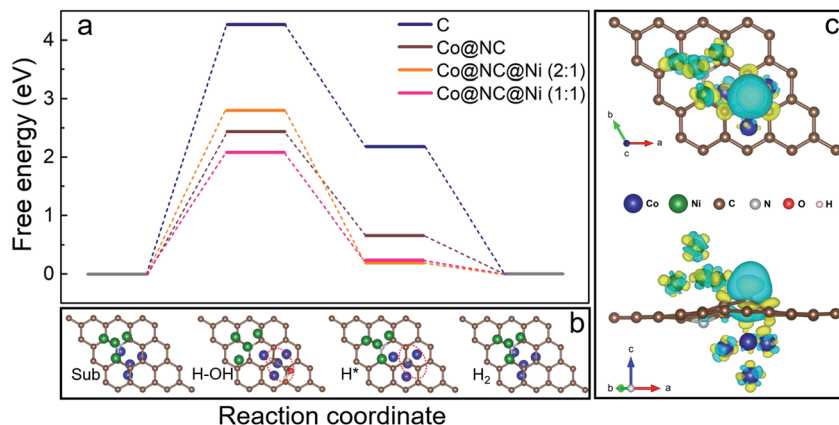


Fig. 4 (a) The calculated free energy profiles of different models in alkaline solution. (b) The structures of predicted intermediates that bind to water and hydrogen. (c) The charge density transfer ($\Delta\rho$) of H adsorbed on the Co@NC@Ni (1 : 1) system. The blue, green, brown, silver, red, and pale-pink balls represent Co, Ni, C, N, O, and H atoms, respectively. The blue and yellow isosurfaces denote electron loss and gain, respectively.

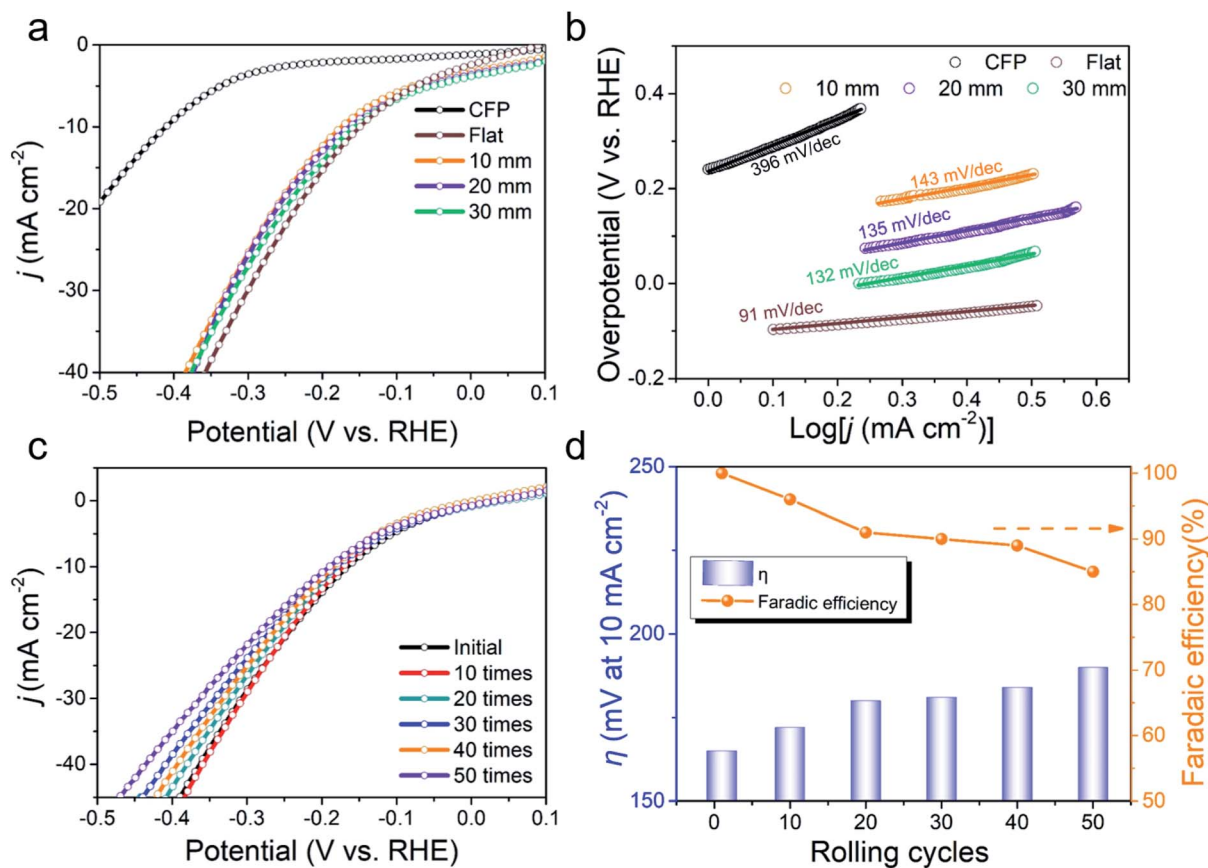


Fig. 5 (a) LSV curves of Co-NCF@600-Ni/CFP flexible electrodes with different rolling diameters. (b) Tafel curves of CFP and Co-NCF@600-Ni/CFP electrodes rolled on Teflon rods with different diameters. (c) LSV curves of the Co-NCF@600-Ni/CFP flexible electrode after repeatedly rolling on a 30 mm diameter rod. (d) Overpotential at a current density of 10 mA cm^{-2} and the faradaic efficiency of the Co-NCF@600-Ni/CFP electrode after repeatedly rolling on a 3 mm diameter rod.

(Video 1, ESI†). The LSV curves (Fig. 5a) show that a current density of 10 mA cm^{-2} is achieved at an overpotential of 160 mV for the catalyst belt on a 30 mm diameter rod, while a negligible increase can be observed on 20 mm diameter (163 mV) and 100 mm diameter (174 mV) rods. The results indicate a better HER performance under lower strain, probably due to the lower number of active sites on the surface being squeezed and covered during deformation.^{79,80} Meanwhile, the flat Co-NCF@600-Ni/CFP belt presents a relatively lower overpotential (150 mV) than the powdery catalyst (157 mV) because of a higher mass loading (about 3 times higher). Previous literature has proved that a large mass loading is beneficial to the catalytic performance.^{69,81,82} The corresponding Tafel slopes (Fig. 5b) suggest that the HER process of these belt catalysts follows a Volmer–Heyrovsky pathway.⁸³ In order to lucubrate the flexibility of the Co-NCF@600-Ni/CFP catalyst, the belt was repeatedly rolled (the details of one rolling step are shown in Video 2, ESI†), and the HER performance was measured after every 10 times rolling. We noticed that the belt was almost cracked with some flaws appearing on the surface after 50 times rolling. The polarization curves and the corresponding Tafel plots (Fig. S19†) show a small increase of overpotential (at 10 mA cm^{-2}) during the repeated rolling, and the faradaic efficiency

maintains a level of 85% after 50 times rolling (Fig. 5c and d). The slight deterioration of the performance can be ascribed to the flaws on the surface, which lead to subtle exfoliation of the active substances into the electrolyte as the digital photo exhibits in Fig. S20.†

4 Conclusions

We have successfully developed a novel and effective strategy to fabricate a dispersed Ni nanograin-anchored Co-NCF by a feasible pyrolysis–ALD approach. Electrochemical measurements demonstrate that the ALD-Ni nanograins can significantly improve the HER performance of the MOF-derived structure. Owing to the properties of ALD, the structure and the electrochemical performance can be intentionally tuned by controlling the size of the Ni nanograins. DFT calculations reveal the electronic tuning among Co/NCF/Ni interfaces, and the introduction of ALD-Ni is beneficial for the HER. Besides, a flexible catalyst device is developed, and the flexible Co-NCF@600-Ni electrode delivers 10 mA cm^{-2} at a low overpotential of 160 mV under a bending situation. A good durability of 50 repeated rolling cycles with a small deterioration of the performance is demonstrated for the flexible device. This

study opens up a new avenue toward the design and fabrication of non-precious metal electrocatalysts in deformable systems. This tactic can be extended to the development of other electrocatalysts for *e.g.* oxygen reduction and carbon dioxide reduction.

Conflicts of interest

The authors declare no competing financial interest.

Acknowledgements

This work was supported by the National Natural Science Foundation of China (No. 51961145108 and 61975035), the Science and Technology Commission of Shanghai Municipality (No. 19XD1400600 and 17JC1401700), and the National Key R&D Program of China (No. 2017YFE0112000).

Notes and references

- M. G. Walter, E. L. Warren, J. R. McKone, Q. M. Boettcher, E. A. Santori and N. S. Lewis, *Chem. Rev.*, 2010, **110**, 6446–6473.
- J. Turner, *Science*, 2004, **5**, 972–974.
- Z. W. Seh, J. Kibsgaard, C. F. Dickens, I. Chorkendorff, J. K. Nørskov and T. F. Jaramillo, *Science*, 2017, **335**, 146–158.
- S. Chu and A. Majumdar, *Nature*, 2012, **488**, 294–303.
- X. Zou and Y. Zhang, *Chem. Soc. Rev.*, 2015, **44**, 5148–5180.
- A. Grimaud, A. Demortière, M. Saubanère, W. Dachraoui, M. Duchamp, M. Doublet and J. Tarascon, *Nat. Energy*, 2017, **2**, 16189.
- S. Cherevko, S. Geiger, O. Kasian, N. Kulyk, J. Grote, A. Savan, B. R. Shrestha, S. Merzlikin, B. Breitbach, A. Ludwig and K. J. Mayrhofer, *Catal. Today*, 2015, **262**, 170–180.
- J. S. Sun, Z. Wen, L. P. Han, Z. W. Chen, X. W. Lang and Q. Jiang, *Adv. Funct. Mater.*, 2018, **28**, 1706127.
- T. S. Zeleke, M. C. Tsai, M. A. Weret, C. J. Huang, M. K. Birhanu, T. C. Liu, C. P. Huang, Y. L. Soo, Y. W. Yang, W. N. Su and B. J. Hwang, *ACS Nano*, 2019, **13**, 6720–6729.
- Q. H. Liang, L. X. Zhong, C. F. Du, Y. B. Luo, J. Zhao, Y. Zheng, J. W. Xu, J. M. Ma, C. T. Liu, S. Z. Li and Q. Y. Yan, *ACS Nano*, 2019, **13**, 7975–7984.
- W. Chen, J. T. Muckerman and E. Fujita, *Chem. Commun.*, 2013, **49**, 8896–8909.
- J. Wang, F. Xu, H. Jin, Y. Chen and Y. Wang, *Adv. Mater.*, 2017, **29**, 1605838.
- N. Mahmood, Y. Yao, J. Zhang, L. Pan, X. Zhang and J. Zou, *Adv. Sci.*, 2018, **5**, 1700464.
- B. Y. Guan, X. Y. Yu, H. B. Wu and X. W. Lou, *Adv. Mater.*, 2017, **29**, 1703614.
- Y. Yang, Z. Lun, G. Xia, F. Zheng, M. He and Q. Chen, *Energy Environ. Sci.*, 2015, **8**, 3563–3571.
- X. You, W. Tu, B. Zhang, S. Yin, Y. Huang, M. Kraft and R. Xu, *Adv. Mater.*, 2017, **29**, 1605957.
- M. Kuang, Q. Wang, P. Han and G. Zheng, *Adv. Energy Mater.*, 2017, **7**, 1700193.
- J. W. Su, Y. Yang, G. Xia, J. Chen, P. Jiang and Q. Chen, *Nat. Commun.*, 2017, **8**, 14969.
- B. Zhu, R. Zou and Q. Xu, *Adv. Energy Mater.*, 2018, **8**, 1801193.
- J. Liu, D. Zhu, C. Guo, A. Vasileff and S. Z. Qiao, *Adv. Energy Mater.*, 2017, **7**, 1700518.
- Y. T. Zhao, G. S. Huang, D. R. Wang, Y. Ma, Z. Y. Fan, Z. H. Bao and Y. F. Mei, *J. Mater. Chem. A*, 2018, **6**, 22870–22878.
- Y. L. Li, Y. T. Zhao, G. S. Huang, B. R. Xu, B. Wang, R. B. Pan, C. L. Men and Y. F. Mei, *ACS Appl. Mater. Interfaces*, 2017, **9**, 38522–38529.
- J. X. Li, W. J. Liu, J. Y. Wang, I. Rozen, S. He, C. R. Chen, H. G. Kim, H. J. Lee, H. B. R. Lee, S. H. Kwon, T. L. Li, L. Q. Li, J. Wang and Y. F. Mei, *Adv. Funct. Mater.*, 2017, **27**, 1700598.
- Y. Mi, L. Y. Wen, Z. J. Wang, D. W. Cao, H. P. Zhao, Y. L. Zhou, F. Grote and Y. Lei, *Catal. Today*, 2016, **262**, 141–145.
- N. C. Cheng, S. Stambula, D. Wang, M. N. Banis, J. Liu, A. Riese, B. W. Xiao, R. Y. Li, T. K. Sham, L. M. Liu, G. A. Botton and X. L. Sun, *Nat. Commun.*, 2016, **7**, 13638.
- P. Nayak, Q. Jiang, N. Kurra, X. B. Wang, U. Buttner and H. N. Alshareef, *J. Mater. Chem. A*, 2017, **5**, 20422–20427.
- Y. M. Kim, D. H. K. Jackson, D. W. Lee, M. Choi, T. W. Kim, S. Y. Jeong, H. J. Chae, H. W. Kim, N. J. Park, H. J. Chang, T. F. Kuech and H. J. Kim, *Adv. Funct. Mater.*, 2017, **27**, 1701825.
- D. H. Kim, J. G. Song, H. M. Yang, H. Y. Lee, J. S. Park and H. J. Kim, *Nanoscale*, 2019, **11**, 844–850.
- Y. Yang, Z. Y. Lin, S. Q. Gao, J. W. Su, Z. Y. Lun, G. L. Xia, J. T. Chen, R. R. Zhang and Q. W. Chen, *ACS Catal.*, 2017, **7**, 469–479.
- N. N. Du, C. M. Wang, X. J. Wang, Y. Lin, J. Jiang and Y. J. Xiong, *Adv. Mater.*, 2016, **28**, 2077–2084.
- D. B. Liu, X. Y. Li, S. M. Chen, H. Yan, C. D. Wang, C. Q. Wu, Y. A. Haleem, S. Duan, J. L. Lu, B. H. Ge, P. M. Ajayan, Y. Luo, J. Jiang and L. Song, *Nat. Energy*, 2019, **4**, 512–518.
- J. Deng, P. Ren, D. Deng and X. Bao, *Angew. Chem., Int. Ed.*, 2015, **54**, 2100–2104.
- Y. Yang, Z. Lun, G. Xia, F. Zheng, M. He and Q. Chen, *Energy Environ. Sci.*, 2015, **8**, 3563–3571.
- T. Ling, T. Zhang, B. Ge, L. Han, L. Zheng, F. Lin, Z. Xu, W. Hu, X. Du, K. Davey and S. Z. Qiao, *Adv. Mater.*, 2019, **31**, 1807771.
- M. Streckova, E. Mudra, R. Orinakova, L. Markusova-Buckova, M. Sebek, A. Kovalcikova, T. Sopcak, V. Girman, Z. Dankova, M. Micusik and J. Dusza, *Chem. Eng. J.*, 2016, **303**, 167–181.
- G. J. Li, E. M. Song, G. S. Huang, R. B. Pan, Q. L. Guo, F. Ma, B. Zhou, Z. F. Di and Y. F. Mei, *Small*, 2018, **14**, 1802985.
- G. J. Li, E. M. Song, G. S. Huang, Q. L. Guo, F. Ma, B. Zhou and Y. F. Mei, *Adv. Funct. Mater.*, 2018, **28**, 1801448.
- S. J. Peng, L. L. Li, X. P. Han, W. P. Sun, M. Srinivasan, S. G. Mhaisalkar, F. Y. Cheng, Q. Y. Yan, J. Chen and S. Ramakrishna, *Angew. Chem.*, 2014, **126**, 12802–12807.

- 39 C. Guan, X. M. Liu, W. N. Ren, X. Li, C. W. Cheng and J. Wang, *Adv. Energy Mater.*, 2017, **7**, 1602391.
- 40 J. P. Perdew and K. Burke, *Phys. Rev. Lett.*, 1996, **77**, 3865–3868.
- 41 J. P. Perdew and K. Burke, *Phys. Rev. Lett.*, 1997, **78**, 1396.
- 42 P. E. Blöchl, *Phys. Rev. B: Condens. Matter Mater. Phys.*, 1994, **50**, 17953–17979.
- 43 G. Kresse and J. Hafner, *Phys. Rev. B: Condens. Matter Mater. Phys.*, 1993, **47**, 558–561.
- 44 G. Kresse and J. Hafner, *Phys. Rev. B: Condens. Matter Mater. Phys.*, 1994, **49**, 14251–14269.
- 45 G. Kresse and J. Furthmüller, *Comput. Mater. Sci.*, 1996, **6**, 15–50.
- 46 G. Kresse and J. Furthmüller, *Phys. Rev. B: Condens. Matter Mater. Phys.*, 1996, **54**, 11169–11186.
- 47 H. J. Monkhorst and J. D. Pack, *Phys. Rev. B: Solid State*, 1976, **13**, 5188–5192.
- 48 H. Hu, L. Han, M. Z. Yu, Z. Y. Wang and X. W. Lou, *Energy Environ. Sci.*, 2016, **9**, 107–111.
- 49 Y. X. Zhang, L. Y. Du, X. F. Liu and Y. Q. Ding, *Nanoscale*, 2019, **11**, 3484–3488.
- 50 J. Deng, P. J. Ren, D. H. Deng and X. H. Bao, *Angew. Chem., Int. Ed.*, 2015, **54**, 2100–2104.
- 51 Z. L. Chen, R. B. Wu, Y. Liu, Y. Ha, Y. H. Guo, D. L. Sun, M. Liu and F. Fang, *Adv. Mater.*, 2018, **30**, 1802011.
- 52 Y. Pan, K. A. Sun, S. J. Liu, X. Cao, K. L. Wu, W. C. Cheong, Z. Chen, Y. Wang, Y. Li, Y. Q. Liu, D. S. Wang, Q. Peng, C. Chen and Y. D. Li, *J. Am. Chem. Soc.*, 2018, **140**, 2610–2618.
- 53 Y. M. Kim, D. H. K. Jackson, D. W. Lee, M. Choi, T. W. Kim, S. Y. Jeong, H. J. Chae, H. W. Kim, N. J. Park, H. J. Chang, T. F. Kuech and H. J. Kim, *Adv. Funct. Mater.*, 2017, **27**, 1701825.
- 54 T. A. Ho, C. D. Bae, H. C. Nam, E. S. Kim, S. Y. Lee, J. H. Park and H. J. Shin, *ACS Appl. Mater. Interfaces*, 2018, **10**, 12807–12815.
- 55 J. P. Shi, D. L. Ma, G. F. Han, Y. Zhang, Q. Q. Ji, T. Gao, J. Y. Sun, X. J. Song, C. Li, Y. S. Zhang, X. Y. Lang, Y. F. Zhang and Z. F. Liu, *ACS Nano*, 2014, **8**, 10196–10204.
- 56 N. Masurkar, N. K. Thangavel and L. R. Arava, *ACS Appl. Mater. Interfaces*, 2018, **10**, 27771–27779.
- 57 Y. Liu, C. L. Liang, J. J. Wu, T. Sharifi, H. Xu, Y. Nakanishi, Y. C. Yang, C. F. Woellne, A. Aliyan, A. A. Martí, B. X. Xie, R. Vajtai, W. Yang and P. M. Ajayan, *Adv. Mater. Interfaces*, 2018, **5**, 1700895.
- 58 C. Maclsaac, J. R. Schneider, R. G. Closser, T. R. Hellstern, D. S. Bergsman, J. Park, Y. Z. Liu, R. Sinclair and S. F. Bent, *Adv. Funct. Mater.*, 2018, **28**, 1800852.
- 59 S. H. Shin, Z. Y. Jin, H. Kwon, R. Bose and Y. E. Min, *Langmuir*, 2015, **31**, 1196–1202.
- 60 D. S. Kong, H. T. Wang, J. J. Cha, M. Rasta, K. J. Koski, J. Yao and Y. Cui, *Nano Lett.*, 2013, **13**, 1341–1347.
- 61 D. H. Kim, J. G. Song, H. M. Yang, H. Y. Lee, J. S. Park and H. J. Kim, *Nanoscale*, 2019, **11**, 844–850.
- 62 X. Zou, X. Huang, A. Goswami, R. Silva, B. R. Sathe and T. Asefa, *Angew. Chem., Int. Ed.*, 2014, **53**, 4372–4376.
- 63 J. Staszak-Jirkovsky, C. D. Malliakas, P. P. Lopes, N. Danilovic and S. S. Kota, *Nat. Mater.*, 2015, **15**, 197–203.
- 64 X. Fan, Y. Liu, Z. Peng, Z. Zhang, H. Zhou, X. Zhang, B. I. Yakobson, W. A. Goddard, X. Guo, R. H. Hauge and J. M. Tour, *ACS Nano*, 2017, **11**, 384–394.
- 65 M. X. Li, Y. Zhu, H. Y. Wang, C. Wang, N. Pinna and X. F. Lu, *Adv. Energy Mater.*, 2019, **9**, 1803185.
- 66 Z. Zhao, S. L. Liu, J. X. Zhu, J. S. Xu, L. Li, Z. Q. Huang, C. Zhang and T. X. Liu, *ACS Appl. Mater. Interfaces*, 2018, **10**, 19871–19880.
- 67 Z. G. Ye, T. Li, G. Ma, Y. H. Dong and X. L. Zhou, *Adv. Funct. Mater.*, 2017, **27**, 1704083.
- 68 Y. Huang, Y. Sun, X. Zheng, T. Aoki, B. Pattengale, J. Huang, X. He, W. Bian, S. Younan, N. Williams, J. Hu, J. Ge, N. Pu, X. Yan, X. Pan, L. Zhang, Y. Wei and J. Ge, *Nat. Commun.*, 2019, **10**, 982–993.
- 69 P. E. Blöchl, Projector Augmented-Wave Method, *Phys. Rev. B: Condens. Matter Mater. Phys.*, 1994, **50**, 17953.
- 70 J. Zhang, *et al.*, *Energy Environ. Sci.*, 2016, **9**, 2789–2793.
- 71 J. Zhang, *et al.*, *Angew. Chem., Int. Ed.*, 2016, **55**, 6702–6707.
- 72 E. Skulason, G. S. Karlberg, J. Rossmeisl, T. Bligaard, V. Greeley, H. Jonsson and J. K. Nørskov, *Phys. Chem. Chem. Phys.*, 2007, **9**, 3241–3250.
- 73 B. Hinnemann, P. G. Moses, J. Bonde, K. P. Jørgensen, J. H. Niesen, S. Horch, I. Nørskov and K. Chorkendorff, *J. Am. Chem. Soc.*, 2005, **127**, 5308–5309.
- 74 J. Deng, P. J. Ren, D. H. Deng, L. Yu, F. Yang and X. H. Bao, *Energy Environ. Sci.*, 2014, **7**, 1919–1923.
- 75 Y. Zheng, Y. Jiao, A. Vasileff and S. Z. Qiao, *Angew. Chem., Int. Ed.*, 2018, **57**, 7568–7579.
- 76 N. Mahmood, Y. Yao, J. W. Zhang, L. Pan, X. Zhang and J. J. Zou, *Adv. Sci.*, 2018, **5**, 1700464.
- 77 V. Sheng, M. Myint, J. G. Chen and Y. Yan, *Energy Environ. Sci.*, 2013, **6**, 1509–1512.
- 78 G. M. Chen and A. M. Zhang, *Presented at IDETC/CIE. Accuracy Evaluation of PRBM for Predicting Kinetostatic Behavior of Flexible Segments in Compliant Mechanisms*, Washington, DC, USA, 2011.
- 79 R. Xu, R. Wu, Y. M. Shi, J. F. Zhang and B. Zhang, *Nano Energy*, 2016, **24**, 103–110.
- 80 L. B. Ma, Y. Hu, R. P. Chen, G. Y. Zhu, T. Chen, H. L. Lv, Y. R. Wang, J. Liang, H. X. Liu, C. Z. Yan, H. F. Zhu, Z. X. Tie, Z. Jin and J. Liu, *Nano Energy*, 2016, **24**, 139–147.
- 81 E. J. Popczun, C. G. Read, C. W. Rosk, N. S. Lewis and R. E. Schaak, *Angew. Chem., Int. Ed.*, 2014, **53**, 5427–5430.
- 82 J. R. McKone, B. F. Samodiftler, C. A. Werlang, N. S. Lewis and H. B. Gray, *ACS Catal.*, 2013, **3**, 166–169.
- 83 Y. Li, H. Wang, L. Xie, Y. Liang, G. Hong and H. Dai, *J. Am. Chem. Soc.*, 2011, **133**, 7296–7299.